POLITECNICO DI TORINO
Repository ISTITUZIONALE

Computationally efficient design procedure for single-layer IPM machines

Original
Computationally efficient design procedure for single-layer IPM machines / Ferrari, S., Pellegrino, G., M Jafar, M.Z., Husain, I.. - ELETTRONICO. - (2019). (2019 International Electric Machines and Drives Conference (IEMDC) San Diego May 12-15, 2019) [10.1109/IEMDC.2019.8785394].

Availability:
This version is available at: 11583/2734212 since: 2019-12-13T15:27:51Z

Publisher:
IEEE

Published
DOI:10.1109/IEMDC.2019.8785394

Terms of use:

This article is made available under terms and conditions as specified in the corresponding bibliographic description in the repository

Publisher copyright
IEEE postprint/Author's Accepted Manuscript

©2019 IEEE. Personal use of this material is permitted. Permission from IEEE must be obtained for all other uses, in any current or future media, including reprinting/republishing this material for advertising or promotional purposes, creating new collecting works, for resale or lists, or reuse of any copyrighted component of this work in other works.

(Article begins on next page)

11 September 2026

Computationally Efficient Design Procedure for Single-Layer IPM Machines

Simone Ferrari, *Student Member, IEEE*,
Gianmario Pellegrino, *Senior Member, IEEE*
Department of Energy "*Galileo Ferraris*"
Politecnico di Torino,
Turin, Italy
Emails: simone.ferrari@polito.it,
gianmario.pellegrino@polito.it

Mohamed Zubair M Jaffar, *Student Member, IEEE*,
Iqbal Husain, *Fellow, IEEE*
FREEDM System Center
North Carolina State University
Raleigh, NC, USA
Emails: mmohame2@ncsu.edu,
ihusain2@ncsu.edu

***Abstract*—Interior Permanent Magnet machines are widely used in several applications thanks to their optimal tradeoff between torque and flux weakening capability figures. Their design process massively relies on the use of optimization algorithms coupled with Finite Elements Analysis, as dictated by the high number of input parameters and the inadequateness of design equations. This paper proposes a faster design flowchart, based on analytical models for V-type IPM machines. The proposed design procedure is validated against FEA results, referring to the known benchmark of the Toyota Prius 2010 electric motor. Although the precision of the results is not comparable to that obtainable with FEA, the proposed closed-form model is useful and insightful during the preliminary stages of the design. The limits of accuracy of the proposed equations are commented critically. Guidelines are given on how to embed the presented approach into a comprehensive design procedure.**

***Index Terms*—Permanent Magnet Machine, Interior Permanent Magnet Machine, Electrical Machine Design.**

I. Introduction

Nowadays, Interior Permanent Magnet (IPM) machines are used in a wide range of applications. The absence of the rotor cage grants higher efficiency compared to induction motors. Moreover the anisotropic rotor results in IPM machines having a higher torque and power density, and wider Constant Power Speed Range (CPSR), in comparison to Surface Mount Permanent Magnet machines. All these features fit with the specifications for traction power train application [1], [2] and contribute to the wide adoption of IPM motors for traction of electric and hybrid vehicles. The typical design procedure for IPM motors involves the massive use of optimization algorithms and Finite Element Analysis (FEA) models. This strategy allows to precisely estimate the machine performance and find trade-offs between several design objectives. However, such computer-based design strategies are extremely time consuming. Analytical models coupled with optimization algorithms reduce the computational effort [3], [4]. However, this is at the cost of reduced accuracy, which is also a function of the geometric inputs. In addition, iterations are needed to account for the non-linear steel curve, which increases the computational time. Altogether, all algorithmic optimization techniques tend to leave a very marginal role to the designer's insight and experience. This work emphasizes the initial analytical design of custom IPM machines and its role in the subsequent computer-based design chain. With a bad initial design, both the number of iterations and the risk of non-optimal results are increased. A closed-form design procedure is presented, based on a simple analytical model, intended for the initial stage of the design process. The results are presented on a design plane where the inputs are the rotor radius normalized to the stator outer radius and magnet length normalized to the airgap length. The goal functions are the output torque and characteristic current referred to the rated current. The latter figure represents the CPSR capability of the IPM machine. The proposed design plane helps the designer in finding a compromise between the design goals, while keeping a general understanding of the machine behavior. Optimization algorithms can be later used to refine the model. Altogether, the proposed solution results in a faster, intuitive and optimal design. The proposed analytical tool is then included in the open-source design tool SyR-e [5].

II. IPM Machine Model

The IPM machine model is expressed as:

$$\begin{cases} \lambda_d = \lambda_{PM} - L_d\, i_0\, sin(\gamma) \\ \lambda_q = L_q\, i_0\, cos(\gamma) \end{cases} \tag{1}$$

where λ_d and λ_q are the flux linkages components, i_0 is the rated current, γ is the phase advance angle of the current vector, with respect to the q-axis, λ_{PM} is the PMs flux linkage and L_d and L_q are inductances along d and q. Each inductance is the sum of two terms: the magnetizing term (L_{md} and L_{mq}) and the leakage term L_σ, equal for both axes. The machine model (1) is then used to compute all the figures of merit as torque (2), characteristic current (3), and so on.

$$T = \frac{3}{2} p \left[\lambda_{PM}\, i_0\, cos(\gamma) + (L_q - L_d)\, i_0^2\, \frac{sin(2\gamma)}{2} \right] \tag{2}$$

$$i_{ch} = \frac{\lambda_{PM}}{L_d} \tag{3}$$

In reality, the three parameters of the model (1) are a function of the current operating point $i_d = -i_0\, sin(\gamma)$ and $i_q =$

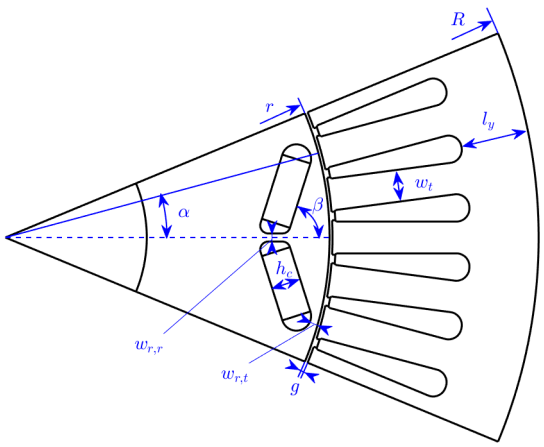

Fig. 1. Machine geometry parameters

$i_0\,cos(\gamma)$. Moreover, in the design stage, some simplifications will be adopted. First, the effect on the parameters of the current on the other axis (the so called cross-saturation) is neglected. This assumption leads to overestimation of torque. Second, the d-axis is considered linear (non-saturating), so L_d and λ_{PM} are not function of i_d. This assumption is in general true in the region of interest (negative i_d, lower module than the characteristic current), this hypothesis results in less than 5% error in the d-axis flux linkage estimate. The model parameters (λ_{PM}, L_d and L_q) derive from the motor geometry and the material characteristics. During the design process, and especially at the initial stage, analytical models can give a good idea of the influence of geometrical changes on the machine model. Magnetic equivalent circuits can be adopted in this stage, as [3], but a careful analysis must be done on the assumptions: a correct analytical model can be precise, at the expense of an augmented parameter numbers, that can be difficult to handle. In the following, analytical formulations are proposed for the machine model according to the geometry of Fig. 1. Table I reports the main parameters of the benchmark machine. In the inductances definitions, it will be convenient to refer L_{md} and L_{mq} values to a common ideal inductance L_{gap}. This is namely the inductance of a isotropic machine with idealized iron, and so it is related to the airgap only. Assuming N_s number of turns in series per phase, a rotor radius r, a stack length L and an airgap g, L_{gap} is defined as:

$$L_{gap} = \frac{6\,\mu_0}{\pi} \cdot \left(\frac{k_w\,N_s}{p}\right)^2 \cdot \frac{r\,L}{k_c\,g} \tag{4}$$

where k_w is the winding factor and k_c is the Carter coefficient.

A. PM flux linkage

The PM flux linkage λ_{PM} is one of the most important parameters of the IPM machines. Assuming linear iron, the PMs produce a square flux density wave at the airgap, as shown in Fig. 2. This assumption holds true usually, because the PMs alone are not able to saturate the iron along the flux path. Moreover, the rotor parameters are sufficient to compute the λ_{PM}. The peak of the square wave can be computed with the equivalent circuit reported in Fig. 3.

TABLE I
KEY PARAMETERS OF THE BENCHMARK MACHINE

Number of pole pairs	p	4
Number of slots per pole per phase	q	2
Magnet span angle [°]	α	15.1
V magnet angle [°]	β	67
Magnet thichness $[mm]$	h_c	7.23
Stator outer radius $[mm]$	R	87.5
Rotor outer radius $[mm]$	r	80.3
Stack length $[mm]$	L	50
Airgap length $[mm]$	g	0.73
Rated current $[A]$	i_0	88
Characteristic current $[A]$	i_{ch}	90
Magnet remanence (@20°C) $[T]$	B_r	1.22
Number of turns in series per phase	N_s	88

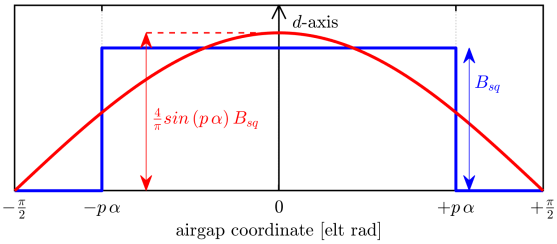

Fig. 2. Shape of the airgap flux density generated by the PMs on one pole pitch (blue) and its first harmonic (red).

Solving the equivalent circuit it results:

$$\Phi_{PM} = B_{sq}\,r\,\alpha = \frac{(B_r\,s_{PM} - B_s\,w_{ribs}) \cdot \frac{h_c}{\mu_0\,s_b}}{\frac{h_c}{\mu_0\,s_b} + \frac{k_c\,g}{\mu_0\,r\,\alpha}} \tag{5}$$

where B_r is the PMs remanence, s_{PM} is the PMs width, s_b is the barrier width (air+PMs), w_{ribs} is the total ribs width in half pole, equal to $w_{ribs} = w_{r,t} + w_{r,r}/2$ and k_c is the Carter coefficient. All the other geometrical quantities are reported in Fig. 1. After some elaboration, B_{sq} can be expressed as:

$$B_{sq} = \frac{B_r \left[\left(1 - \frac{w_{r,t}+\frac{h_c}{2}}{r}\right) k_\alpha - \frac{\frac{w_{r,r}}{2} + \frac{B_s}{B_r}\,w_{ribs}\,sin(\beta)}{r\,\alpha}\right]}{sin(\beta) + \frac{k_c\,g}{h_c}\,k_\alpha} \tag{6}$$

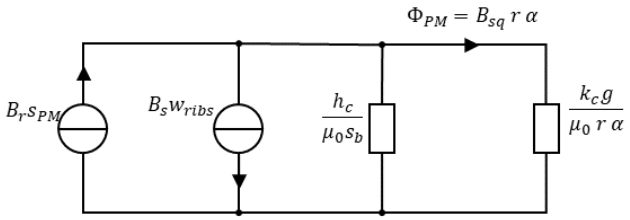

Fig. 3. Magnetic equivalent circuit of half pole (unit stack length), for the PM flux linkage computation.

where k_α is defined as:

$$k_\alpha = \frac{sin\,(\alpha)}{\alpha} \tag{7}$$

After the peak of the airgap flux density is computed, the PM flux linkage λ_{PM} is evaluated as:

$$\lambda_{PM} = \frac{2\,r\,L\,k_w\,N_s}{p} \cdot \left[\frac{4}{\pi} \cdot sin\,(p\,\alpha) \cdot B_{sq}\right] \tag{8}$$

The term in square brackets of (8) defines the peak of the fundamental in the no-load airgap flux density $B_{g,PM}$ (see Fig. 2), while the other terms are obtained by integrating $B_{g,PM}$ over one electrical period along the airgap.

B. d-axis magnetizing inductance

The d-axis magnetizing inductance L_{md} is computed using the equivalent circuit reported in Fig. 4. For this model, iron is considered ideal and the ribs are assumed saturated by the PMs. It follows that the pole can be divided in two flux tubes not connected to each other. The first path includes the flux barrier and the airgap above the barrier (respectively green and blue sections in Fig. 4), while the other path incorporates the airgap in the interpolar region (red section). Considering that L_{md} is not affected by PMs, their effect can be neglected in the model. This is valid because of the ideal iron hypothesis, justify the use of the superposition principle. The two Magneto-Motive Forces (MMFs) that supplies the two circuits are computed by averaging the fundamental stator MMF over the two airgap sections. Assuming the peak stator MMF equal to $\mathcal{F}$, it follows:

$$f_1 = \frac{\int_0^{p\,\alpha} \mathcal{F}\,cos(x)\,dx}{p\,\alpha} = \frac{2}{\pi}\,\mathcal{F}\,\frac{sin(p\,\alpha)}{\frac{2p\,\alpha}{\pi}} \tag{9}$$

$$f_2 = \frac{\int_{p\,\alpha}^{\frac{\pi}{2}} \mathcal{F}\,cos(x)\,dx}{\frac{\pi}{2} - p\,\alpha} = \frac{2}{\pi}\,\mathcal{F}\,\frac{1 - sin(p\,\alpha)}{1 - \frac{2p\,\alpha}{\pi}} \tag{10}$$

Assuming the PMs permeance equal to that of air, the reluctances are computed from the geometry, and result in:

$$\mathcal{R}_{g,1} = \frac{k_c\,g}{\mu_0\,r\,L\,\alpha} \tag{11}$$

$$\mathcal{R}_{g,2} = \frac{k_c\,g}{\mu_0\,r\,L\,\left(\frac{\pi}{2\,p} - \alpha\right)} \tag{12}$$

$$\mathcal{R}_b = \frac{h_c}{\mu_0\,r\,L\,\frac{sin(\alpha)}{sin(\beta)}} \tag{13}$$

According to the superposition principle, the average flux linkage Φ_{md}, needed for the inductance computation, is equal to the sum of the fluxes of the two paths Φ_1 and Φ_2. It results in:

$$\Phi_{md} = \left[\mathcal{F}\,\mu_0\,\frac{r\,L}{k_c\,g}\,\frac{\pi}{2p}\right] \cdot \left\{1 - \frac{sin(p\,\alpha)\,\frac{sin(\beta)}{k_\alpha}}{\frac{k_c\,g}{h_c} + \frac{sin(\beta)}{k_\alpha}}\right\} \tag{14}$$

The first term of (14) represents the average flux linkage if only the airgap is considered and it is at the base of L_{gap} computation. The L_{md} is then easily computed in per-unit of L_{gap} as the ratio between Φ_{md} and this flux linkage, resulting in:

$$\frac{L_{md}}{L_{gap}} = 1 - \frac{sin(p\,\alpha)\,\frac{sin(\beta)}{k_\alpha}}{\frac{k_c\,g}{h_c} + \frac{sin(\beta)}{k_\alpha}} \tag{15}$$

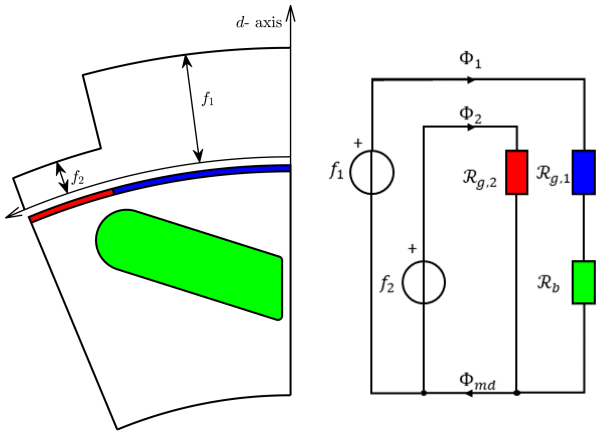

(a) (b)

Fig. 4. Magnetizing d-axis inductance model: real geometry and weighting factors (a) and magnetic equivalent circuit (b).

C. q-axis magnetizing inductance

In principle, if iron is assumed ideal, the only contribution to the magnetizing inductance comes from the airgap, and so $L_{mq} = L_{gap}$. This hypothesis is far from being true: the finite iron magnetic permeability leads to a lower q-axis inductance than the ideal case. Furthermore, the non-linear $B - H$ steel characteristic leads to a complex model, usually solved with iterative methods, as [4].

An easier method can be used in the design stage. The rotor saturation is neglected, because it is not possible to predict the flux paths in the rotor a priori. The most saturated stator sections are considered, as proposed in [6] for SyR machines. The critical sections, where the iron is considered not ideal, are the portion of the stator yoke spanning half of slot pitch (red in Fig. 5) and one stator tooth (blue in Fig. 5). Since the inductance in inversely proportional to the reluctance, L_{mq} value, is computed through the total q-axis reluctance, referred to the airgap reluctance, and then:

$$\frac{L_{mq}}{L_{gap}} = \frac{\frac{2\,p\,k_c\,g}{\mu_0\,\pi\,r}}{\frac{2\,p\,k_c\,g}{\mu_0\,\pi\,r} + \frac{l_t}{\mu_t\,w_t} + \frac{\pi}{\mu_y\,3\,p\,q}\left(\frac{R}{l_y} - \frac{1}{2}\right)} \tag{16}$$

To estimate L_{mq}, the magnetic permeabilities in the different iron sections (μ_t for the tooth and μ_y for the yoke) must be estimated. Since the model is non-linear, an iterative solution is needed. However, a simplified and closed-form method to estimate the $B - H$ curve working point will be introduced during the design procedure flowchart.

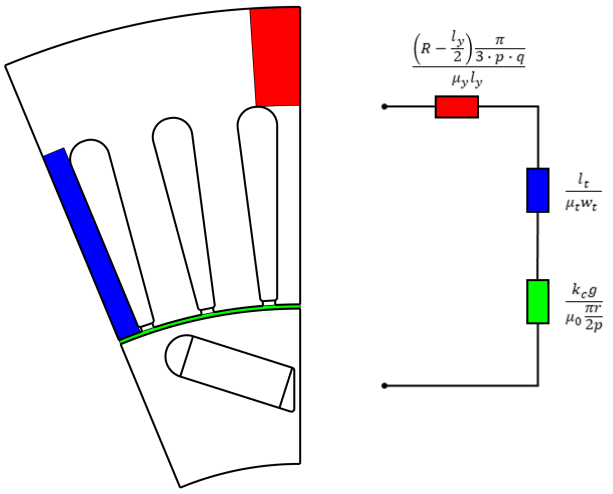

(a) (b)

Fig. 5. Magnetizing q-axis inductance model: real geometry (a) and magnetic equivalent circuit for unit stack length (b).

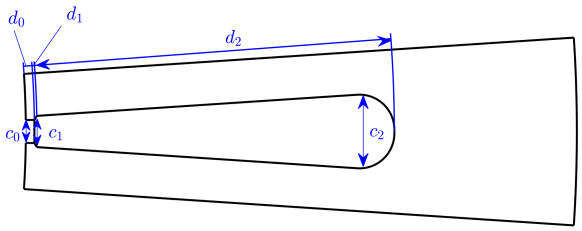

Fig. 6. Definition of the slot dimensions for the leakage inductance computation.

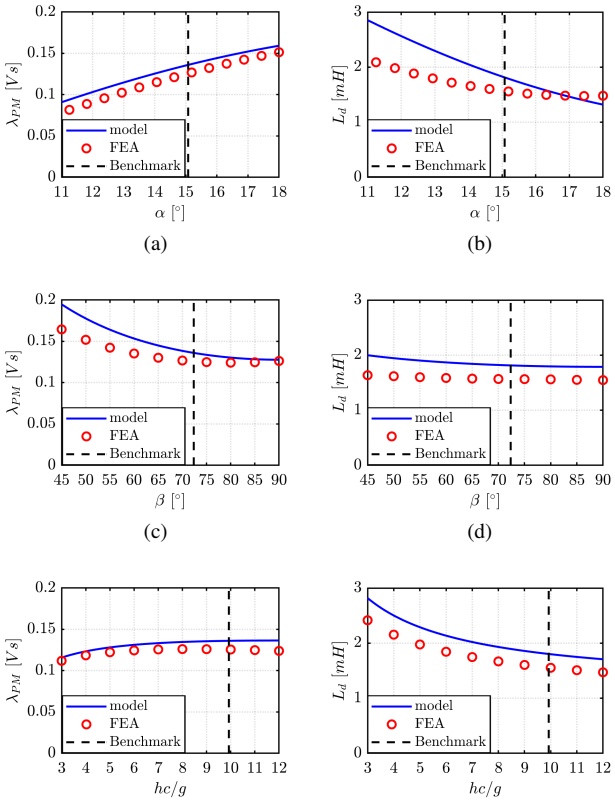

Fig. 7. Sensitivity analysis of d-axis quantities (λ_{PM} and L_d) versus rotor parameter (α_{pu}, β and h_c/g), evaluated with the proposed model (blue line) and FEA (red dots).

D. Leakage inductance

The leakage inductance L_σ is equal on both the d and q axes and is dominated by the slot leakage term. The adopted model is derived in [7]. Assuming a single layer winding and referring to the slot dimensions defined in Fig. 6, the slot leakage inductance is:

$$L_\sigma = \frac{2\,\mu_0\,N_s^2\,L}{p\,q}\,p_s \tag{17}$$

where p_s is the permeance factor of the stator slot. Assumed $\xi = c_1/c_2$, the permeance factor p_s is computed as:

$$p_s = \frac{d_0}{c_0} + \frac{d_1}{c_0}\,\frac{ln(\frac{c_1}{c_0})}{\frac{c_1}{c_0}-1} + \frac{d_2}{c_2}\,\frac{\xi^2 - \frac{\xi^4}{4} - ln(\xi) - \frac{3}{4}}{(1-\xi)(1-\xi^2)^2} \tag{18}$$

E. FEA validation of L_d and λ_{PM} estimates

Starting from the benchmark machine defined in Table I, and by sweeping α, β and h_c/g a series of machines are investigated with the proposed analytical model and with FEA simulations. The aim is twofold: first, the precision of the proposed model is verified for a range of possible designs and not just for one design; then, the effect of the rotor geometry on the magnetic model parameters is investigated, giving important guidelines for the design procedure. The considered parameters are just the d-axis quantities (λ_{PM} and L_d). The q-axis inductance cannot be computed off-line because the estimation of the iron working point is related to the design procedure, so its model will be verified later. The FEA-computed λ_{PM} is measured in no-load condition, as for the analytical model, while the L_d simulations are set with PM and the current only on the d-axis ($i_q = 0$). In this way, cross-saturation is not considered, as for the analytical model. Fig. 7 reports the results of the analysis. In general λ_{PM} is always well estimated, except for a higher overestimation for low values of β (Fig. 7c). For these designs, PM flux concentration is excessive and saturation effects occur. The PM flux linkage is mainly affected by α and β, while it is less sensitive to h_c variations. Regarding L_d, the model is precise against β and h_c variation, but is less precise against α variations. Moreover, in good designs, α is as high as possible in order to increase λ_{PM}. For these designs, L_d model is more precise and robust. The d-axis inductance is quite insensitive to β variations, while it can be changed by changing α or h_c.

III. Parametric Design Plane

The base of the proposed design procedure is the T versus i_{ch} design plane. The two axes of the plane are two dimension-

less parameters: the rotor-stator split ratio $x = \frac{r}{R}$ and the PM-airgap length ratio $\frac{h_c}{g}$. On the plane, the performance figures are reported as function of the two design parameters, helping the designer choose the best trade-off design. The selected performance figures are torque T (2) and the characteristic current $\frac{i_{ch}}{i_0}$ (3). Each couple of coordinates of the plane corresponds to one design. The common input parameters are:

- Stack sizes: outer stator radius R and stack length L;
- Airgap length g;
- Number of pole pairs p and number of slots per pole per phase q;
- PM remanence B_r.

In addition, two loading factors are imposed. They are the peak iron flux density at open circuit B_{Fe} and the thermal loading factor k_j. The former defines the stator sizing and gives an idea of how much the PMs are important for the motor. Lower B_{Fe} compared to the iron saturation point results in lower λ_{PM} compared to the rated flux linkage and higher anisotropy contribution to the total motor torque. The latter is defined as the rated copper loss divided by the stator outer surface (19) and gives an idea of the capability of the cooling system to extract heat from the machine.

$$k_j = \frac{\frac{3}{2} R_s \, i_0^2}{2 \pi R L} \tag{19}$$

A. Design procedure

The design procedure is repeated for each point on the design plane and consists of several steps.

1) **Rotor design**. The first step is to define the rotor parameters. They are the PM span α and the PM angle β. The latter is designed to have the highest L_{mq}, by trying to mimic the circular barrier shape, typical of SyR machines [6]. The adopted criteria for the PM span α design is to set the iron thickness between two barriers of two consecutive poles, equal to the tooth width. Therefore, the tooth width w_t must be designed. Assuming a tooth factor k_t, its design equation is obtained by imposing the no-load iron flux density in the tooth.
$$w_t = \frac{2\pi r}{6 p q} k_t \frac{B_{sq}}{B_{Fe}} \tag{20}$$
In turn, B_{sq} is function of α and β (6). So, all the quantities are written function of α, and the correct α value is solved from the consistent equation. As a consequence, β, B_{sq} and w_t are fixed.
2) **Stator design**. After the rotor definition, B_{sq} is known, and the stator can be sized. Tooth width was computed in the previous step using (20), and the yoke length l_y is computed, under similar assumptions, as:
$$l_y = \frac{\pi}{2} \cdot \frac{r}{p} \cdot \frac{B_{sq}}{B_{Fe}} \cdot \left(\alpha \frac{2p}{\pi} \right) \tag{21}$$
This completely defines the stator. Therefore, the slot leakage inductance L_σ is computed using (17).
3) **Rated current computation**. The rated current i_0 is computed starting from the thermal loading factor k_j, by inverting (19). It results in:
$$i_0 = \sqrt{k_j \cdot \frac{k_{Cu}}{\rho} \cdot \frac{L}{L + l_{end}} \cdot \frac{\pi R A_{slots}}{9 N_s^2}} \tag{22}$$
Where l_{end} is the end-turn length, ρ is the copper resistivity and A_{slots} is the total slot area, computed after the stator design. Then, the dq-axis currents $i_d = -i_0 \, sin(\gamma)$ and $i_q = i_0 \, cos(\gamma)$ can be computed, by imposing $\gamma = 45°$, that is a raw estimation of the Maximum Torque per Ampere (MTPA) condition for IPM machines.
4) ***d*-axis parameters and characteristic current**. With stator and rotor completely defined, the d-axis parameters λ_{PM} and L_d can be evaluated. The former is computed through (8), while the latter is evaluated as the sum of the d-axis magnetizing term and the leakage term, as mentioned in the previous section. Now, the first figure of merit, the characteristic current i_{ch}, can be evaluated.
5) **Saturated *q*-axis inductance**. Now, the q-axis inductance can be computed, using (16). The magnetic permeabilities μ_y and μ_t should be estimated with a complex and iterative procedure because of the non-linear relation between the flux density B (proportional to the flux linkage) and the magnetic field H (proportional to the current). Despite that, the design procedure drive to a simplified estimation method, avoiding iterative process. The method is graphically described in Fig. 8 for the yoke section and can be repeated for tooth by using the proper flux density. According to the design constraint, the iron flux density at no load condition is equal to $B_{y,ini} = B_{Fe}$ in the yoke section and $B_{t,ini} = B_{Fe}/k_t$ in the tooth. This saturation condition will be addressed as "initial" condition in the following (with subscript ini). Since the working point on the steel curve is known, it is possible to compute the magnetic fields $H_{y,ini}$ and $H_{t,ini}$, as well as the magnetic permeabilities $\mu_{y,ini}$ and $\mu_{t,ini}$. Neglecting the structural ribs, the initial condition in the stator core can be roughly obtained by removing the PMs and injecting the characteristic current i_{ch} on the d-axis. In this way, B level in the iron is related to a d-axis current value. The next step is to compute the q-axis current able to induce the initial condition. Because of the rotor anisotropy, it results in:
$$i_{q,ini} = i_{d,ini} \frac{L_d}{L_{q,ini}} = i_{ch} \frac{L_{md} + L_\sigma}{L_{mq,ini} + L_\sigma} \tag{23}$$
where $L_{mq,ini}$ is the q-axis magnetizing inductance in the initial condition, computed with (16) and using $\mu_{t,ini}$ and $\mu_{t,ini}$. Now, a link between the iron working point and the q-axis current is established, and the load working point in the iron sections can be estimated.

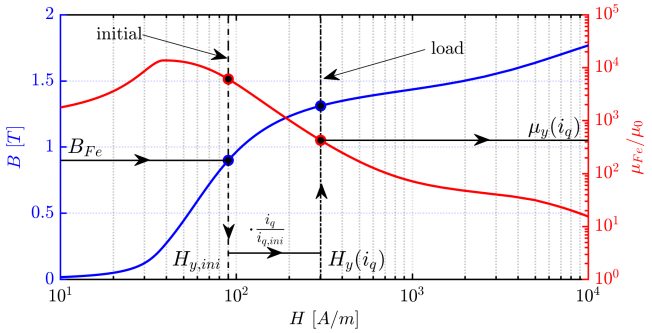

Fig. 8. Steel saturation estimation along the q-axis for the yoke section

TABLE II
COMPARISON BETWEEN THE BENCHMARK AND THE TWO DESIGNED MACHINES

	Benchmark	**Mot1**		**Mot2**	
Method	FEA	Model	FEA	Model	FEA
x	0.608	0.608		0.58	
hc/g	9.9	9.9		6	
α [°]	15.07	16.42		17.55	
β [°]	72.35	67.35		64.53	
i_0 $[A]$	89.8	81.0		86.6	
T $[Nm]$	103.0	110.8	95.9	109.1	97.7
i_{ch} $[A]$	89.8	99.2	101.0	87.4	81.7

Since H is proportional to the current, the magnetic field in load condition (neglecting cross saturation) is:

$$H_k = H_{k,ini} \frac{i_q}{i_q, ini} \tag{24}$$

where $k = y$ denotes the yoke working point, and $k = t$ denotes the tooth working point, both at load condition. The magnetic permeabilities μ_y and μ_t is then easily obtained from the material curve by interpolation, and the L_{mq} at load is finally estimated.

6) **Design plane**. At the end, torque can be computed using (2) and the design plane can be plotted, as shown in Fig. 9. Torque contours highlight a high torque region at the center of the plane. For higher x, slots became smaller, and the rated current decrease, reducing torque production. While for lower x the rated current is higher, but λ_{PM} is reduced because of the smaller rotor radius. Regarding the h_c/g effect, it is less evident that x. In general, high h_c/g value means thicker PM, so an higher B_{sq}, and then a thicker back iron, reducing the slot area, and then the rated current. Similar comments can be done regarding the characteristic current: it exists a curve almost in the middle if the plane where $i_{ch} = i_0$ and then ideally infinite CPSR. If x or h_c/g increase, λ_{PM} increase, while L_d and i_0 decrease, increasing i_{ch}/i_0.

B. Selected Test Case

The input parameters reported in Table I, taken from the Toyota PRIUS 2010 case, are used to show how the proposed design procedure works: Fig. 9 reports the design plane obtained starting from such parameters, common to all the

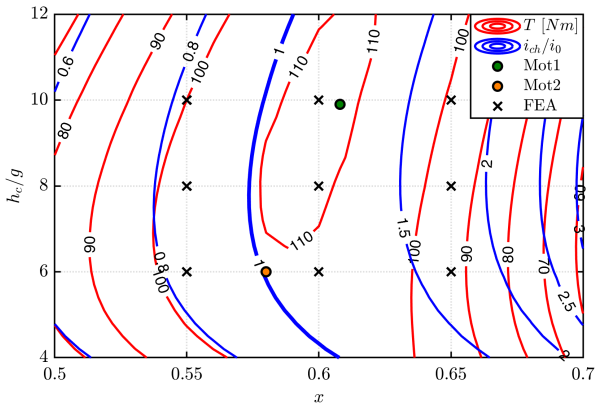

Fig. 9. Parametric design plane: torque T and characteristic current i_{ch} function of the design parameters.

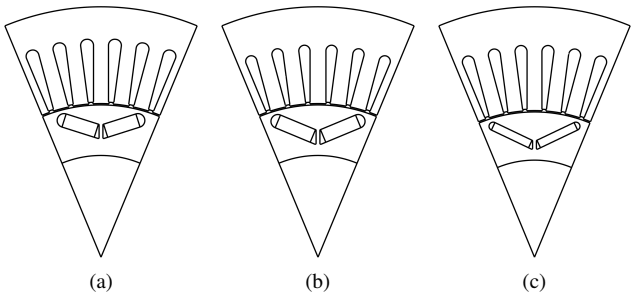

Fig. 10. Comparison of the benchmark (a) with the two motors selected on the parametric plane: Mot1 (b) and Mot2 (c)

considered designs (same stack dimensions, same number of poles, same copper losses etc ..).

Two machines are picked from the plane, to show the effects of the design parameters. The first, called Mot1, has the same x and h_c/g of the benchmark machine. Mot1 geometry is slightly different from the benchmark machine because the the latter is optimized, while the former is just the first step of the design. A second machine (named Mot2) is selected on the design plane, to show how the design parameters affect the motor geometry. Mot2 presents an estimated torque similar to Mot1, with a characteristic current closer to the rated current. The two motor geometries are compared in Fig. 10. Mot1 presents the same rotor radius and the same PM's thickness of the benchmark machine, while PM's span and angle are different because of the optimization algorithm. As for the definitions, Mot2 has a smaller rotor of Mot1 (because of the lower x), and thiner PMs, according to the input parameters. Moreover, PM's span and angle and stator dimensions are recomputed with the proposed procedure and are different for the two machines. Table II compares the performance figures of the two designed machines with the optimized benchmark. The table reports both the analytical model and FEA results for the proposed designs. The flux linkage is slightly overestimated, as stated in the previous section. Besides the smaller rotor radius, Mot2 flux linkage is similar of Mot1 because

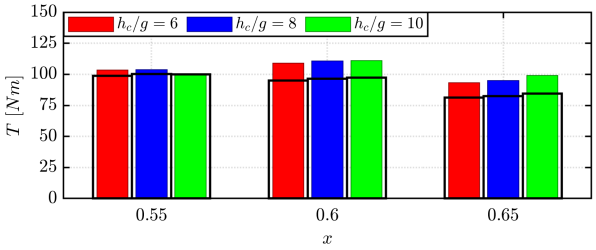

(a)

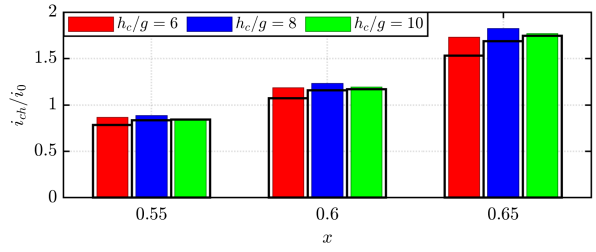

(b)

Fig. 11. Comparison between model estimation (colored bars) and FEA simulations (transparent bars) for the nine FEA-analyzed machines: torque (a) and characteristic current (b).

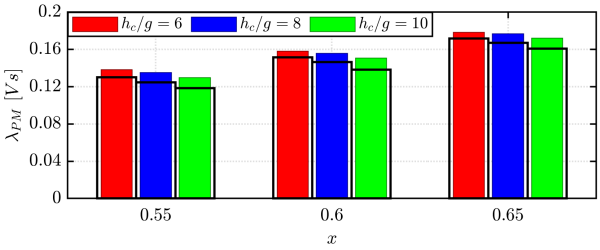

(a)

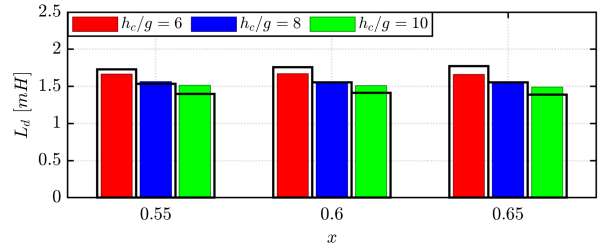

(b)

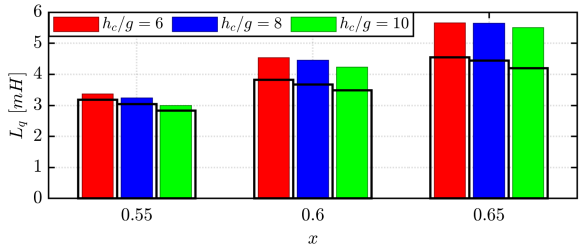

(c)

Fig. 12. Comparison between model estimation (colored bars) and FEA simulations (transparent bars) for the nine FEA-analyzed machines: PM flux linkage (a), d-axis inductance (b) and q-axis inductance (c).

of the different PM span angle. The characteristic current is overestimated by about $10\,A$ for both the models, because of the lower precision of the L_d estimation. Further details on the model precision will be discussed later. Characteristic current is higher than the benchmark machine for both the designed motors because of the higher PM flux linkage. Regarding torque, the estimation error is about 10% for both designs. This is mainly due to saturation and cross-saturation, as will be addressed later. A further comment on the results of the design plane must be done by comparing the machine picked from the plane with the benchmark motor. Mot1 is one of the best candidate from the design plane and it is quite similar to the benchmark. Obviously, the benchmark performances are better: higher torque and virtually infinite CPSR. However, it is also the results of a long and time-consuming optimization process, while the design plane takes few tens of seconds to be computed. The design plane enables an extremely fast estimation of several designs, at the cost of a non-optimal precision. Besides the accuracy compared with FEA, the design plane allows to find the trade-off design, that could be further FEA evaluated and optimized.

C. FEA Validation Across the Design Plane

The precision of the design equations is investigated by FEA-evaluating nine machines from the design plane. The machines lie on a regular grid close to the center of the design plane, as reported with black crosses in Fig. 9. The performance figures computed with the proposed model are compared with FEA results in Fig. 11, while the model parameters are compared in Fig. 12. They are λ_{PM}, computed at no-load, L_d, computed in the characteristic current condition ($i_d = -i_{ch}$, $i_q = 0$) and L_q, computed at load condition. From the analysis, it results that torque is in general overestimated. Torque error grows with x, with a maximum error of 17%. This trend is caused by the inaccuracy of the L_q estimation (Fig. 12c), that is overestimated because of iron saturation. Besides the estimation errors, the torque trend, function of x and h_c/g, is well predicted: the analytical model is able to detect the high torque designs. Regarding the characteristic current, the precision is in general higher than torque. The q-axis inductance does not affect i_{ch}, and the error is not proportional to x as for torque. Characteristic current estimation is inaccurate for low values of h_c/g, while is precise for thicker PMs. This behavior is caused by the errors of the d-axis parameters involved in i_{ch} estimation. The PM flux linkage is always overestimated, with an error between 3% and 7%, while L_d is underestimated for low h_c/g and overestimated elsewhere. This cause the different error in i_{ch}: if the two parameters are both overestimated, a compensation effect takes place, and the error on the performance figure is lower. Conversely, if one parameters is overestimated and the other is underestimated, the error is not balanced and the i_{ch} accuracy is penalized. This behavior will be discussed later. Nevertheless, the proposed model results enough precise in

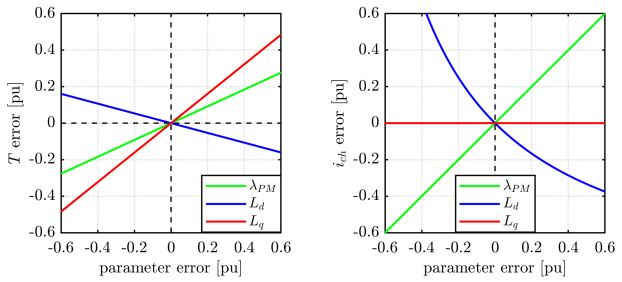

(a) (b)

Fig. 13. Effect of the model parameters errors on the performance figures.

i_{ch} estimation for the good design area. Actually, machines with low h_c/g values are prone to demagnetization issues, and are less advised than machines with thicker PMs, as for the benchmark example ($h_c/g = 9.9$). In conclusion, the proposed analytical model is less precise than FEA, but can effectively adopted in the preliminary design stage to identify the best designs. To improve the model accuracy, a hybrid analytical-FEA approach can be adopted, as done for SyR machines in [6]. This strategy can dramatically improve the model precision, at the cost of a longer computational time, that is still much lower than optimization procedures.

D. Sensitivity Analysis

To further investigate the model precision, the effect of the parameters error on the performance figures is addressed. The results of the analysis are summarized in Fig. 13. According to the results from the previous analysis, torque error is nearly proportional to L_q error. Moreover, a compensation effect could be partially given by L_d. The d-axis inductance in load condition is lower than the L_d computed in the previous analysis, because of the cross-saturation. This side effect make the L_d always overestimated for torque computation, balancing the L_q error. For this reason, torque error is lower than L_q error in the previous analysis. Considering the other performance figure, i_{ch} error is proportional to λ_{PM} error and inversely proportional to L_d error. This analysis confirms the compensation effect observed in the previous analysis: characteristic current is more precise if the two d-axis parameters are both overestimated of the same percentage, while if the error sign is opposite, the i_{ch} precision is penalized.

IV. Conclusion

In this paper, a fast design procedure for single layer, V-type rotor IPM machines was presented. The design procedure is based on the torque and characteristic current plane, where the latter is index of the flux weakening capability of each design. The two performance figures are estimated using an analytical model, less accurate but extremely faster than FEA simulations. Of the two goal functions, the most critical to be estimated is the output torque. This is mostly related to the imprecision of the L_q parameter, variable with saturation and current phase angle. Conversely, the results reported for the per-unit characteristic current are encouraging, and represent, in the authors' opinion, the main contribution of the paper. FEA is used to validate the model and design procedure, highlighting a level of precision adequate to the preliminary design stage. Besides accuracy, the key contribution is the ability to identify the area of the plane where the machines having the best trade-off between torque and flux weakening capability reside. This feature, applied to the preliminary design stage, can reduce the computational effort of an optimization algorithm to converge to the optimal design. By way of the proposed design plane, the designer can have a preliminary estimate of which designs comply with the flux weakening (that is constant power speed range) requirements of the application, and cross that area of the plane with the one of maximum torque designs. Such information is useful even in absence of a precise torque estimate, provided that the torque trends are respected across the plane. The proposed design flowchart is then included in the design tool SyR-e.

References

[1] Y. Yang, S. M. Castano, R. Yang, M. Kasprzak, B. Bilgin, A. Sathyan, H. Dadkhah, and A. Emadi, "Design and comparison of interior permanent magnet motor topologies for traction applications," *IEEE Transactions on Transportation Electrification*, vol. 3, no. 1, pp. 86–97, March 2017.

[2] T. A. Burress, S. L. Campbell, C. L. Coomer, C. W. Ayers, A. A. Wereszczak, J. P. Cunningham, L. D. Marlino, L. E. Seiber, and H. T. Lin, "Evaluation of the 2010 Toyota Prius hybrid synergy drive system,," report ORNL/TM-2010/253.

[3] E. C. Lovelace, T. M. Jahns, and J. H. Lang, "A saturating lumped parameter model for an interior PM synchronous machine," in *IEEE International Electric Machines and Drives Conference. IEMDC'99. Proceedings (Cat. No.99EX272)*, May 1999, pp. 553–555.

[4] M. Z. M. Jaffar and I. Husain, "Path permeance based analytical inductance model for IPMSM considering saturation and slot leakage," in *2017 IEEE International Electric Machines and Drives Conference (IEMDC)*, May 2017, pp. 1–7.

[5] F. Cupertino, G. Pellegrino, and et al., "SyR-e: Synchronous Reluctance (machines) - evolution," accessed 24-January-2019. [Online]. Available: https://sourceforge.net/projects/syr-e/

[6] S. Ferrari and G. Pellegrino, "FEA-augmented design equations for synchronous reluctance machines," in *2018 IEEE Energy Conversion Congress and Exposition (ECCE)*, Sep. 2018, pp. 5395–5402.

[7] T. A. Lipo, *Introduction to AC machine design*. John Wiley & Sons, 2017.